Indian Journal of Pure & Applied Physics
Vol. 62, September 2024, pp. 743-758
DOI: 10.56042/ijpap.v62i9.11602

Effects of Niobium and Vanadium on the Properties of Porous TiMoCuAg High-Entropy Alloys

Ghalia A Gaber[a], Lamiaa Z Mohamed[b*], Omayma A Elkady[c], Ayman H Elsayed[c] & Shimaa A Abolkassem[c]

[a]Department of Chemistry, Faculty of Science (Girls), Al-Azhar University, Yousef Abbas Str., Nasr City, P.O. Box: 11754, Cairo, Egypt
[b]Mining, Petroleum, and Metallurgical Engineering Department, Faculty of Engineering, Cairo University, Giza 12613, Egypt
[c]Powder Technology Department, Manufacturing Technology Institute, Central Metallurgical R and D Institute, P.O. 87, Helwan, Cairo 11421, Egypt

Received 4 June 2024; accepted 1 August 2024

Powder metallurgy was used to create porous TiMoCuAgV HEA (VHEA) and TiMoCuAgNb HEA (NbHEA) using 0, 10, and 20 wt.% from ammonium hydrogen carbonates (AHCs) as a space holding material. Samples were mixed with AHCs as a foaming agent. All samples were compacted at 400 MPa and sintered at 1250^{o}C. X-ray diffraction, scanning electron microscopy, and energy dispersive analyses were performed for phase identification, microstructure observation, and elemental composition, respectively. Fabricated HEAs density values were estimated according to Archimedes' principle. Also, hardness and Young's modulus were determined. The addition of vanadium (V) was shown to exceed that of niobium (Nb) in increasing the HEA Young's modulus without AHCs. The corrosion characteristics of the prepared HEAs in corrosive media were estimated by the weight loss (WL) method, indicating good improvement by adding either V or Nb. The findings showed that the 10-NbHEAs in SBF had the highest improvement values, where the CR value was 0.94 mm/y lower than other investigated media. Additionally, 10-VHEAs in a simulated body fluid solution (SBF) and hydroxyapatite (HA) corroded more rapidly than 10-NbHEAs. After the corrosion test, the surface morphology showed a protective layer for 10-NbHEAs in SBF media. Also, the surface morphology is well-defined as smooth and uniform in HA media for 10-NbHEAs and 20-NbHEAs, which agrees with WL and corrosion rate values. Generally, VHEAs have higher corrosion resistance than NbHEAs.

Keywords: High entropy alloys; TiMoCuAgV HEA; TiMoCuAgNb HEA; Hardness; Microstructure

1 Introduction

The continuous improvement of metallic biomaterials with biocompatibility and proper mechanical properties is urgently required. Due to their high strength, microhardness, ductility, and corrosion resistance, highentropy alloys (HEAs) have earned attention recently[1]. Using multiple elements in HEAs enhances configurational entropy, only when stabilizing the solid solutionstate[2,3]. Richard's rule states that entropy grows as components increase[4]. In the uniform electron gas theory, each mole of an ideal monoatomic gas contains 1.5 R (where R is the gas constant) of internal energy[5]. HEAs play a crucial role in overcoming the shortcomings of traditional alloys in applications where operating load and temperature are very demanding[6,7]. For instance, the use of HEAs in the biomaterial field has proven insufficient progress, and there is a substantial requirement for the next generation of biomaterials research[8]. HEAs have significant configurational entropy, leading to single or two-phase alloys with face-centered cubic (FCC) and body-centered cubic (BCC) structures[9-12].

Solid-state transformations are typical when using high-energy ball milling to prepare HEAs[13-16]. This results in metallic alloys becoming increasingly promising for bone tissue regeneration and support applications[17-19]. Consequently, metals are often selected in orthopedic and orthodontic therapies to sustain failing tissue as temporary and permanent implants[20]. Stainless steels, CoCr alloys, and Ti alloys are the most popular metallic biomaterials because of their superior mechanical characteristics[21-23]. Ti was introduced to HEAs because of its excellent biocompatibility and strength[24-26]. Total hip replacements employ Ti64 metallic implants to rebuild bone and heal arthritic hip joints. The application of Ti64 alloy reduces stress shielding problems in bones due to its low elastic modulus[27,28]. However, it has inadequate wear resistance and third-body abrasion sensitivity. The low wear resistance of

*Corresponding author: (E-mail: Lamiaa.zaky@cu.edu.eg)

the surface oxide layer's low shear strength makes it unsuitable as a bearing support surface[29,30]. Given these factors, Co Cr-based alloys with higher hardness and wear resistance, compared to Ti64, should be used to build implants with porous surface layers[31,32]. A porous layer of Ti alloys atop CoCr alloys diminishes the stress-shielding effect around the implant-bone interface, where bone tissue and implants are linked more effectively than on a porous layer of CoCr alloys[29]. Porous materials play a significant role in various biomedical applications due to their unique properties. These materials possess interconnected pores or void spaces that allow for the exchange of fluids, gases, and biomolecules[33-35]. The specific choice of material and design depends on the intended application, desired properties, and compatibility with biological systems. Ongoing research is continuously exploring new porous materials and optimizing their structures for enhanced biomedical performance. While porous materials offer many advantages for biomedical applications, several challenges need to be addressed. Porous materials often have reduced mechanical strength compared to their dense counterparts. Adjusting the porosity and pore size distribution may be necessary to enhance the mechanical stability of porous materials. Optimizing the material composition, controlling degradation rates, and designing appropriate pore structures are necessary to maintain the structural integrity of porous materials. Addressing the different challenges requires interdisciplinary efforts involving materials scientists, engineers, and biologists. Ongoing research focuses on developing new fabrication techniques, improving material properties, and optimizing the design of porous materials to overcome the challenges in biomedical applications[33-35].

This fact shows one advantage of using porous substrates compared to fully dense specimens, whose mechanical properties are far from those of cortical bone tissue. Thus, the fabrication of porous substrates using the space holder technique produces HEAs substrates with a biomechanical and bio-functional balance[36].

However, pitting corrosion in physiological fluids might accelerate wear degradation in Ti-based amorphous alloys during tribocorrosion[30]. Therefore, recent biomedical material research has concentrated on producing excellent corrosion and wear-resistant implant alloys. Bio-HEAs outperformed pure Ti and Ti64 alloys regarding biocompatibility and mechanical strength[37]. The bio-HEAs typically included Ti, Nb, and Mo as the most essential alloy additions[38,39]. Their high corrosion resistance in simulated human fluids generated a protective surface layer on metals. The thick oxide layer prevents metal ions from dissolution and restricts corrosive agents' damage to the acceptor. Mo, Nb, and other easily passivated elements also improve the alloy's oxide deposit's chemical stability[40,41]. Ti has a hexagonal close-packed structure, whereas Ag has an FCC one, with clear similarities between FCC and HCP stacking sequences. Ti and BCC-structured Nb often produce asolid solution[42]. Metallic ions like Ag and Cu are biocompatible and antimicrobial[18,43]. A previous study has shown potential bactericidal effects with low cytotoxicity for metallic implants containing 1–9% Ag dopants[44,45].

Biomedical applications employing metals are less biocompatible because they corrode, harming the implant and surrounding tissue and organs[46-48]. In degenerative situations, the oral cavity's pH may be 2.0–3.0[49]. Thus, much scientific research has examined HEA corrosion resistance in severe human body environments[50].

This investigation aims to fabricate novel porous materials suitable for bio-medical applications by PM technique. The two bio-HEAs' density, hardness, Young's modulus, microstructure, chemical composition, and phase structure were investigated. Also, it aims to study the corrosion resistance of the two sintered bio-HEAs TiMoCuAgVHEAs (VHEAs) and TiMoCuAgNbHEAs (NbHEAs) in physiological media such assimulated body solution (SBF), hydroxyapatite (HA) and artificial saliva (AS).The surface morphology of the corroded HEAs with different conditions was investigated in different media.

2 Experimental Works

2.1 Materials and Fabrication

Ti, Mo, Cu, Ag, V, and Nb powders with purities of 99.8, 99.9, 99.7, 99.2, 99.9 and 99.9% respectively, are used. All powders were supplied from "Dop company", except for Nb powder, which was prepared by crushing Nb flakes into small pieces using a vibrating disc crushing machine and then converted into a fine powder using a Spex mill with 800 rpm and a 10:1 ball-to-powder ratio for 30 min. Porous VHEAs and NbHEAs with 0, 10, and 20 wt. % foaming agents were prepared via PM. Mechanical

mixing for 2 h was performed ona spex mill with 800 rpm under a controlled argon atmosphere. It was then mixed with ammonium hydrogen carbonate (AHCs) as a foaming agent. All samples were compacted at 400 MPa and sintered at 1250 ℃ in a tube furnace with an Argon environment to prevent oxidation. Table 1 contains the chemical compositions of the manufactured HEAs. According to the Archimedes principle, the constructed specimen's density was estimated. HEAs' phase structure and composition were examined using X-ray diffraction (XRD) with Cu kα radiation (λ=0.15406 nm, 45 V, and 40 mA),(PRO PAN analytical diffractometer, X'Pert, Almelo, Netherlands).The microstructures of the as-received powder and sintered HEAs were analyzed using a scanning electron microscope (SEM) (Quanta 250 FEG, FEI Company, Eindhoven, Netherlands)with energy-dispersive X-ray analysis (EDX) to evaluate the chemical composition distribution. The Vickers hardness of the specimens was determined as the average of ten measurements along the polished cross-sectional surface by applying a 2 kg force for 15 seconds. Young's modulus was assessed by the pulse-echo technique at 5 MHz frequency at room temperature using a Mettler H 72 balance with a capacity of 160 g and an accuracy of 0.1 mg. Also, an Ultrasonic Flaw Detector was used in model USM3.The Young's modulus and Poisson ratio values of 0-VHEA and 0-NbHEA were measured using the pulse-echo technique at 5 MHz frequency at room temperature (RT).

2.2 Corrosion Characteristics

Chemical techniques were developed to assess the corrosion feature of VHEAs and NbHEAs in physiological media like artificial saliva (AS), simulated body fluid (SBF), and HA) media. The chemical composition of AS is KH_2PO_4 0.34 g/L, $NaHPO_4.2H_2O$ 0.445 g/L, $KHCO_3$ 1.5 g/L , NaCl 0.585 g/L, $MgCl_2.6H_2O$ 0.0305 g/L, citric acid 0.0315 g/L and $CaCl_2$ 0.0166 g/L. Meanwhile, the composition of SBF is NaCl 142 g/L, KCl 5 g/L, $MgCl_2$ 1.5 g/L, $CaCl_2.6H_2O$ 2.5 g/L, $NaHCO_3$ 4.2 g/L, K_2HPO_4 1 g/L, and Na_2SO_4 0.5 g/L. Additionally, the composition of the HA is $Ca_5(OH)(PO_4)_3$. Weight loss (WL) measurements of VHEAs and NbHEAs with 0, 10, and 20 wt% foaming agents were done in a glass vessel with 20 ml of different physiological media. The VHEAs or NbHEAs were suspended and weighted (W_2) in the different physiological media. After 24, 48, 72, 96, and 120 h, the HEAs were collected, cleaned with distilled water, dried with acetone, and reweighed (W_2). The difference in the weight of the two sintered bio-HEAs before and after exposure to the corrosive medium are calculated from Eq. 1[51].

$$\Delta W = W_1 - W_2 \quad \text{... (1)}$$

The corrosion rate (CR) of VHEAs or NbHEAs in the different physiological media for a 120h immersion test at RT can be measured by Eq. (2)[52].

$$CR(mm/y) = \frac{\Delta W * K}{A * T * D} \quad \text{... (2)}$$

Where K denotes a constant ($8.76x10^4$), T indicates exposure time in hours, A denotes area in cm^2, ΔW represents the difference in specimen weight before and after immersion in different test solutions, and D means the density of sintered bio-HEAs in g/cm^3 (6.85 g/cm^3 for TiMoCuAgV and 7.33 g/cm^3 for TiMoCuAgNb). The density values of HEAs were estimated using the rule of mixture based on elemental densities.SEM and EDX analyses were used to examine the surface morphology of the corroded HEAs.

3 Results and Discussion

3.1 Thermodynamic Parameters

The mixing of VHEAs and NbHEAs was done at a composition set according to Hume-Ruttery's criterionto anticipate the creation of the solid solution. Table 2 displays the theoretical thermodynamic parameters forecasting the solution's solid appearance.

Table 1 — Chemical compositions of the different fabricated HEAs in at. %

HEAs	Elements, at. %					
	Ti	Mo	Cu	Ag	V	Nb
VHEA	27	27	23	5	18	0
NbHEA	27	27	23	5	0	18

Table 2 — Thermodynamic parameters for VHEAs and NbHEAs

HEAs	ΔH_{mix} (kJ/mol)	ΔS_{mix} (J/K.mol)	VEC	∑ciri	δ	Ω	ΔS_{mix} /R
TiMoCuAgV	-4.86	12.48	6.23	1.39	7.88	5.33	1.50
TiMoCuAgNb	-1.47	12.48	6.23	1.40	7.54	19.19	1.50

The atomic-size parameter (δ), electronegativity difference (Δχ), valence electron concentration (VEC), and Ω parameter of regular melt-interaction are based on the previously provided data[53,54]. Notably, the ΔS_{confg} and ΔH_{mix} parameters represent the configurational entropy and the mixture enthalpy. Zhang *et.al*. have hypothesized that thesolid solution is formed when $-15 < \Delta H_{mix} < 5$ kJ/mol. In addition, using atomic radii $\delta \leq 6.6\%$ as a criterion for SDS formation is also considered. Mixing δ (atomic size differences) and ΔH_{mix} strongly suggests creating a solid solution[54].

It is noted that solid solution calculations are based on the melting points and the chemical ratios of the constituent components. Few experiments concerning high entropy alloys are known to be produced utilizing PM. Numerous PM-related studies have extensively used the high-energy ball milling technique, which provides adequate diffusion to prepare the alloy. This paper suggests a straightforward method for producing HEA alloys based on the theoretical calculations of the parameters for mixing elements (Ti, Mo, Cu, Ag, Nb, and V), which shows that a solid solution may be formed. Since a mixing solution has a more stable thermodynamic state, the mixture's enthalpy implies that no intermetallic compound is generated. The optimal way to anticipate the development of FCC, BCC, and (FCC/BCC) dual phase is the average valence electron concentration (VEC)[55,56]. The phase tends to be FCC when VEC is equal to or more than 8, and the BCC phase becomes stable when VEC is less than 6.87, while the dual FCC and BCC phases become stable when VEC falls between 6.87 and 8. VEC values of 6.28 for TiMoCuAgV and 6.28 for TiMoCuNb show that the BCC phase predominates in Nb and V alloys.

Table 2 reveals that ΔH_{mix} , ΔS_{mix} , Ω and δ%have a higher value than 6.6% for both VHEAs and NbHEAs, which does not satisfy Zhang's criterion for a stable solid solution. HEAs have a mixing enthalpy ranging from -1.47 to -4.86 KJ/mole. However, the mixing entropy of the two alloys is constant. As it is more than 1.1, it encourages the presence of a solid solution. If it is less than one, it enables the existence of intermetallic compounds. According to Table 2, Ω promotes the development of the solid solution phase. When the $\Delta S_{mix}/R$ is more than 1.5, the alloy is referred to as HEA, and when the value lies between 1 and 1.5, this is referred to as a medium entropy alloy "MEA". In the case of the current work,$\Delta S_{mix}/R$(where R is the gas constant) is equivalent to 1.5, indicating that these alloys are HEAs.

3.2 Powder Characterization

Figure 1 shows the powders having different particle sizes, which were used to prepare the alloys. Ti and Mo particles are irregular, with 30 µm and 10 to 100 µm particle sizes, respectively. However, Cu particles have a spiky shape with a 50 µm average particle size. Ag particles have a potato-shaped morphology with an average particle size of 300 µm. V and Nb particles also have irregular shapes with an average particle size of 50 and 15 µm, respectively.

3.3 Sintered HEAs characterization

3.3.1 Density Measurement

Figure 2 shows the density variation of sintered VHEAs and NbHEAs by adding different amounts of AHCs. The AHCs are considered a foaming agent, which dissociates during the sintering process into ammonia (NH_3) and carbon dioxide CO_2that evolves and is released ata slow rate from the samples during the sintering process, forming the porous structure. Two phenomena have been observed by adding AHCs, the first is the decreasing of density with increasing AHCs wt. % for both HEA samples. Secondly, the density of NbHEAs is more affected by adding AHCs compared to the density of VHEAs, which means that NbHEAs have more porosity than the V samples. The effect of AHCs on the prepared samples is remarkably observed by adding 20 wt. % from it, leading to 47 and 38% porosity for NbHEAs and VHEAs respectively. However, there is a small change in the relative density by adding 0 and 10 wt. % from AHCs to the prepared HEAs from the two series. However, the decrease in density values may return to the number of pores formed by the effect of AHCs. Where, the number of pores is higher for NbHEAs, compared to VHEAs. The increase in NbHEAs density values may also return to the presence of Nb elements, stabilizing β-Ti. During the sintering process, the Nb with small particle size is dispersed uniformly and hence acts as a barrier to β-Ti, which limits grain growth and increases density[57]. Mo's excellent solubility with other elements enhances matrix bonding and intermixing, boosting bulk density[2]. The micro and macro pores that form during the sintering process are formed due to the presence of space holder materials and the sintering process[50].

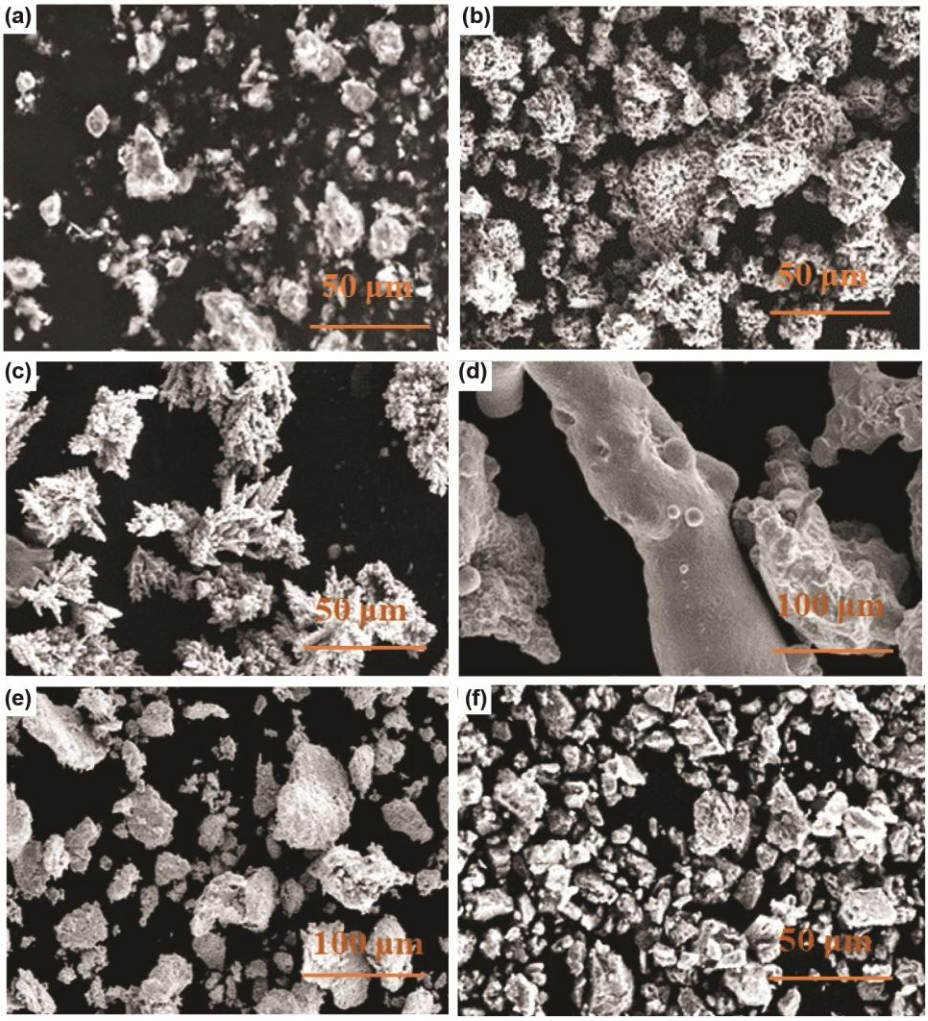

Fig. 1 — SEM micrographs for (a) Ti, (b) Mo, (c) Cu, (d) Ag, (e) Nb, and (f) V powders.

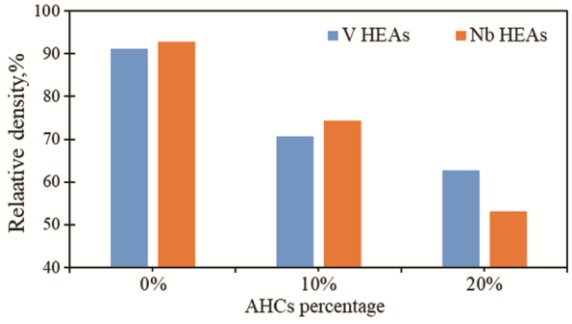

Fig. 2 — Relative density percentages vs. different AHCs percentage of VHEAs and NbHEAs.

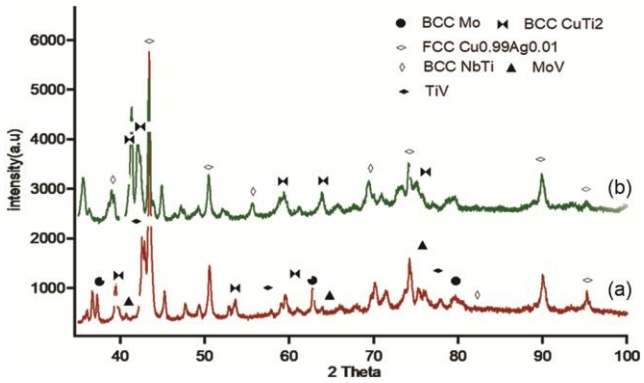

Fig. 3 — XRD analysis for (a) VHEAs and (b) NbHEAs without AHCs material.

3.3.2 XRD Analysis

Figure 3 shows the XRD results for the surface of the manufactured VHEAs and NbHEAs without adding AHCs. Many phases are formed during the sintering process, which indicates complete sintering and good homogeneity between the constituents. FCC structure is the major phase formed, while traces of other phases having BCC structure also form, agreeing well with the thermodynamic calculations. The high entropy effect from mechanical mixing reduces the Gibbs free energy, allowing the development of phases. The chemical compositions

and the processing temperatures of the HEAs' resulted in the entropy responsible for the alloys to form multi-phases. XRD verified the formation of FCC and BCC phases, which causes high mechanical and physical properties of HEAs.

3.3.3 Microstructure Investigation

Figure 4 provides the SEM images for VHEAs and NbHEAs with various percentages of space holder AHC. Two main phases can be seen: the light gray Mo-rich phase, and the darker one, which belongs to V in the case of VHEAs as indicated by EDX, as shown in Figs. 5 & 6.The gray phase is rich with Mo and Nb particles for NbHEAs, while the white spots are rich with Cu element. As indicated by EDX mapping results for both alloys (Fig. 7), homogenous distributions of all elements can also be observed. This suggests the absence of any element segregation due to the good mechanical milling and suitable sintering parameters. In general, the distribution of the constituent elements in the prepared alloys returns to the heat of mixing according to Gibbs's free energy equation[52]. Moreover, the homogenous distribution for pores in both alloys can be observed. It is remarkably observed that the pores are smaller in size for 10-NbHEAsand 10-VHEAs compared to 20-NbHEAs and 20-VHEAs, respectively, which is lower in number but more significant in size, as seen in Fig. 8. In addition, the number of pores increases by increasing the space holder percentage, where the average size of pores is nearly 100 µm in all cases.

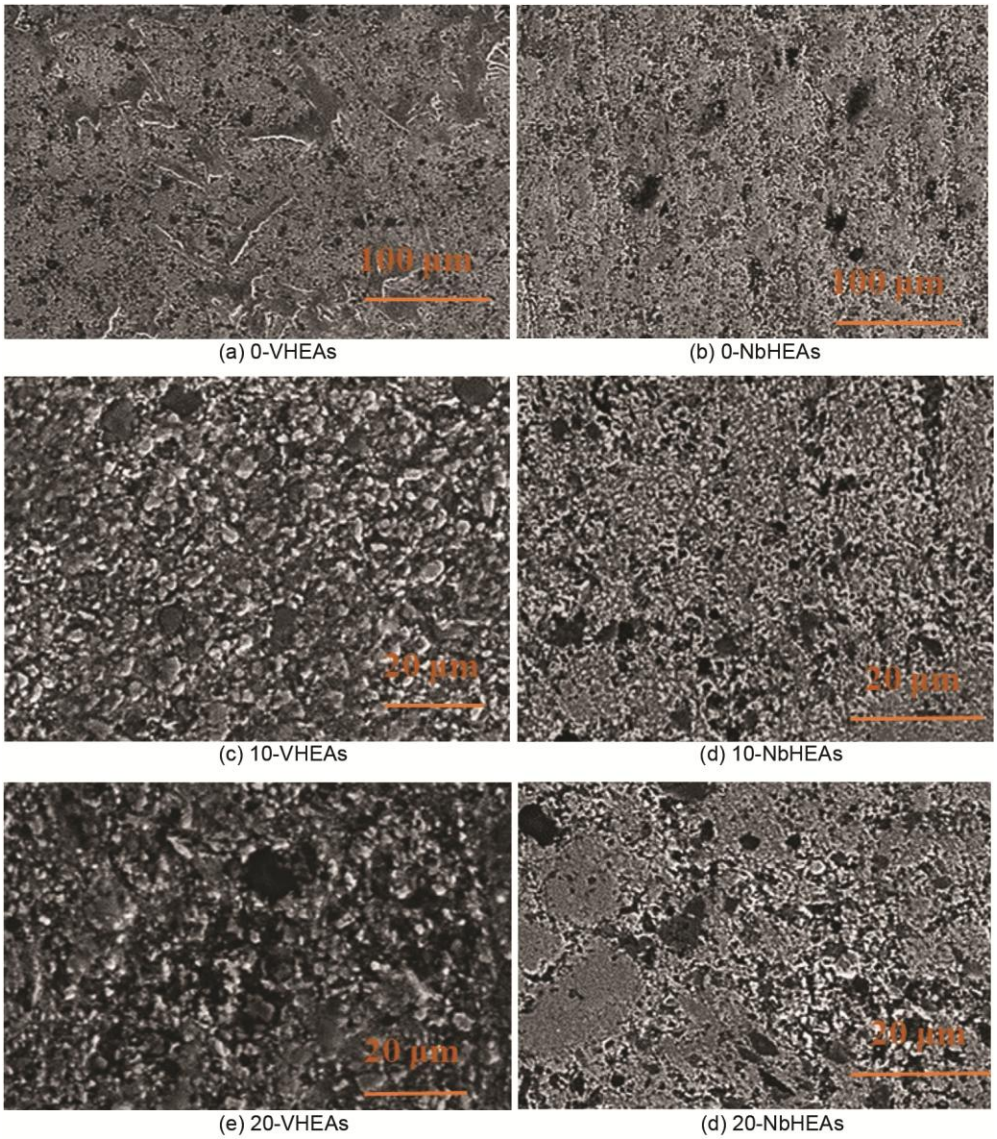

(a) 0-VHEAs (b) 0-NbHEAs

(c) 10-VHEAs (d) 10-NbHEAs

(e) 20-VHEAs (d) 20-NbHEAs

Fig. 4 — SEM micrographs of porous VHEAs and NbHEAs with different percentages of AHCs.

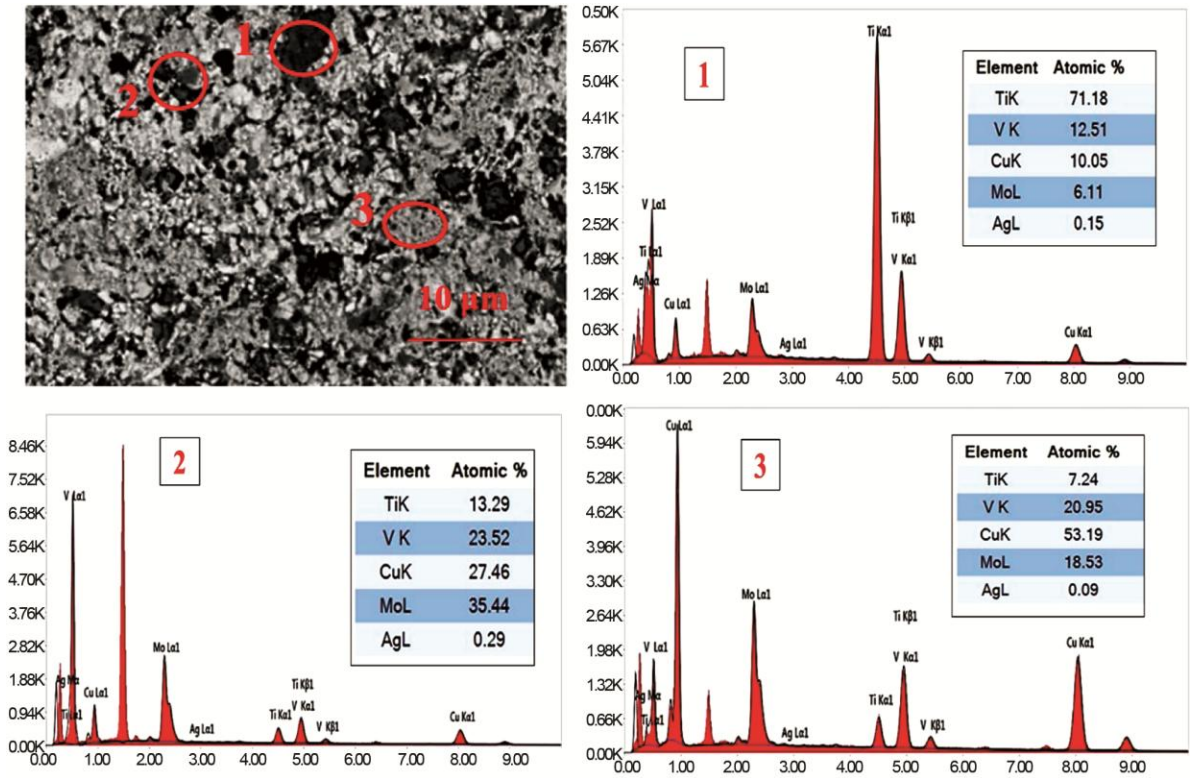

Fig. 5 — SEM image and EDX analyses for 10-VHEAs.

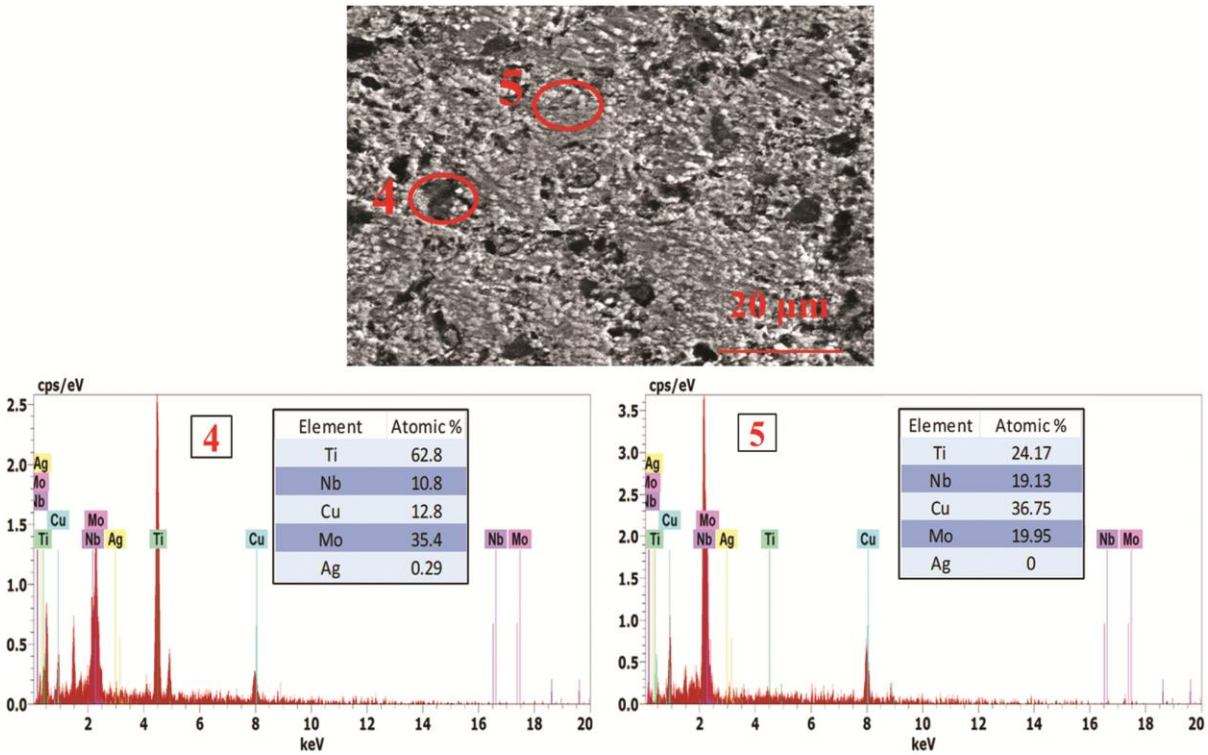

Fig. 6 — SEM image and EDX analysis for 10-NbHEAs.

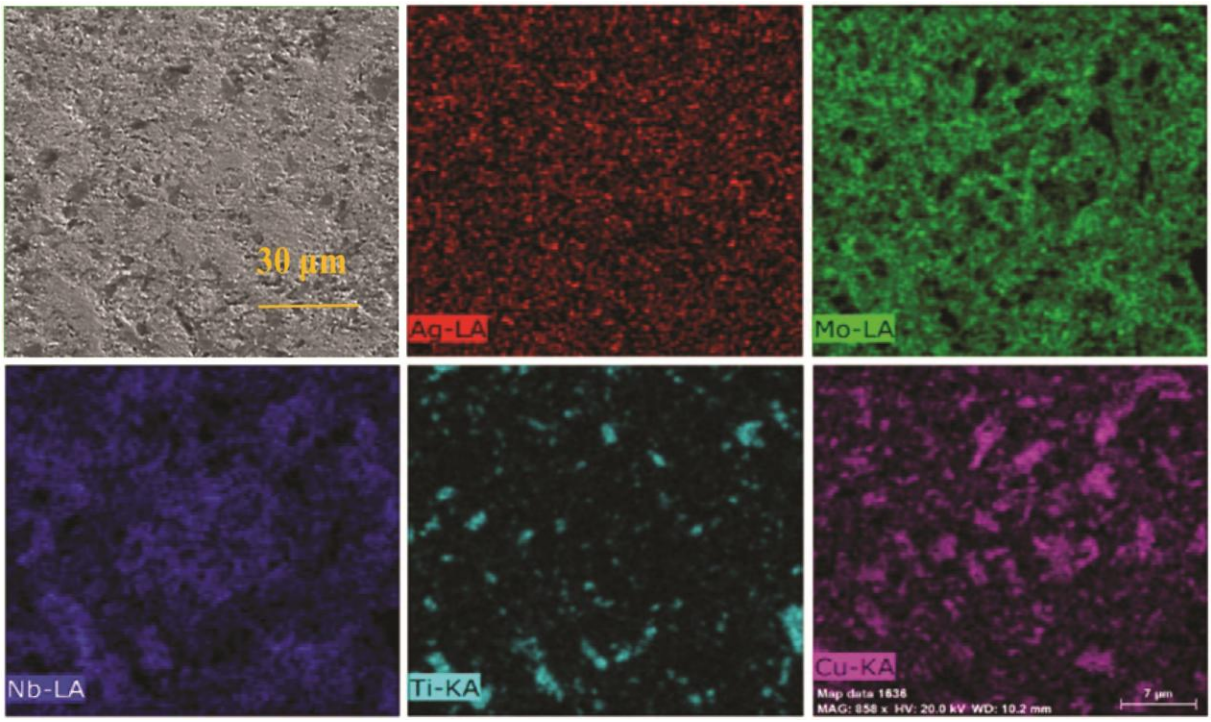

Fig. 7 — Mapping of 10-NbHEAs.

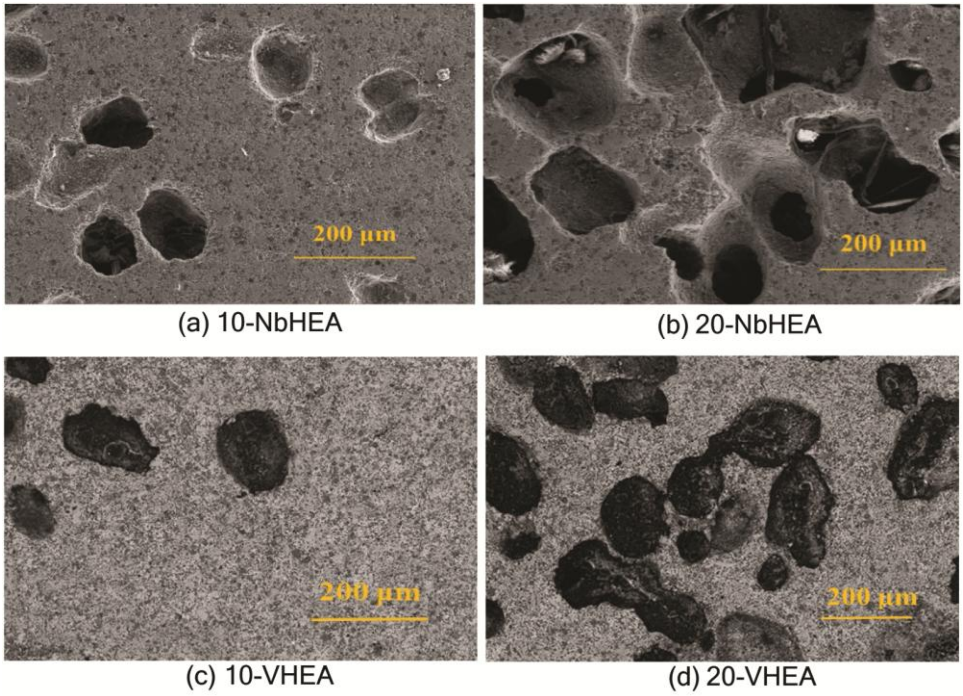

Fig. 8 — Shape of porosity in NbHEAs and VHEAs.

Meanwhile, the microstructure of sintered HEAs without AHCs contains open porosity distributed uniformly throughout the matrix. AHCs create open and closed pores. Points of interactions exist between powder particles, and insufficient heat energy/time for full diffusion and sintering causes open porosity. Some significant open pores were found in the microstructure. Open pores improve surface wettability and tissue development, while closed porosity decreases Young's modulus and implant

failure through stress shielding. Closed porosity voids cannot increase surface wettability or cell adhesion since they are separated[58].

From EDX analysis, it can be observed that the elements with nearly similar temperatures exit in the same phase, as shown in Figs 5, 6 & 7. For example, in the case of VHEA, the main phase (gray) includes Mo with a high melting temperature of about (2610 ℃). At the same time, the darker phase is V-rich with a melting point of 1910 ℃. However, in the case of NbHEA, the main phase includes Mo and Nb. This is because the melting point of Nb is 2477 ℃, near the Mo element.

3.3.4 Hardness Measurements and Young's Modulus Values

Figure 9 shows the Vickers microhardness measurements for VHEAs and NbHEAs under 2 Kg load. It can be seen from the figure that, As the AHCs proportion increases, hardness decreases progressively for both alloys. There is a clear difference between hardness for 0-VHEAs and 10-VHEAs but the hardness is almost similar for 0-NbHEAs and 10-NbHEAs. However, 20-NbHEAs havelower hardness values (100 HV) than VHEAs (180 HV).This explains that the effect of AHCs has developed when added at a high percentage. The trend mentioned above of hardness gradual decrease agrees with density measurement, in which NbHEAs have a higher density than VHEAs in the first two samples. Meanwhile, the higher hardness of NbHEAs may also be due to the higher solubility of Nb with Ti element, which leads to the stabilization of Ti preventing the formation of TiC. The Ti has a strong affinity for carbon to generate primary Ti carbides, which act as an internal barrier to densification and eventually reduce density. Also, the poor miscibility of Ti with Mo greatly influences densification characteristics

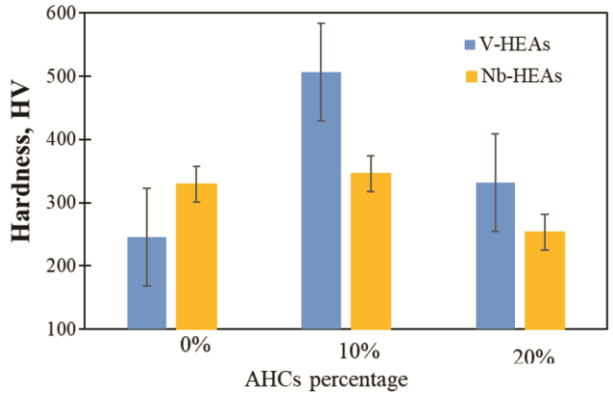

Fig. 9 — Hardness measurement vs. different AHC percentages in VHEAs and NbHEAs.

which remarkably perform at higher percentages from AHCs hence decreasing the density and consequently hardness decreases by increasing the number of pores[2]. In addition, the hardness of VHEAs and NbHEAs are 260 and 273 HV, which is a little far from the hardness of Ti6Al4V, which is 320HV, despitepores and decreased density[59]. Moreover, the high hardness of the alloys may be due to the solid solution strengthening. Hardness also matches density observation, as samples with high-density values have high hardness values. As porosity rises, hardness diminishes because pores collapse under stress.

Young's modulus is a measure of a material's stiffness or its resistance to deformation under an applied force. Traditional metallic biomaterials like stainless steels and titanium alloys have well-established Young's moduli. However, HEAs are unique due to their complex composition and microstructure, which can result in a wider range of mechanical properties. The Poisson's ratio is a mechanical property that describes the ratio of lateral strain to axial strain when a material is subjected to applied stress. The 316L stainless steel is commonly used in medical devices and implants. The Young's modulus of stainless steels is typically around 200 GPa and the Poisson's ratio is around 0.3. Titanium and its alloys, such as Ti-6Al-4V and Ti-6Alk-7Nb alloys, are widely used in orthopedic and dental implants due to their excellent biocompatibility and mechanical properties. The Young's modulus of titanium and its alloys ranges from 100 to 120 GPa and the Poisson's ratio ranges from 0.3 to 0.35. It is important to note that these values are approximate ranges and can vary depending on the specific composition, processing, and testing conditions[60]. The Poisson's ratio is influenced by factors such as the material's structure, porosity, and loading conditions[61]. The Young's modulus and the Poisson ratio of the 0-VHEA and the 0-NbHEA were calculated using the ultrasonic technique, and the results can be found in Table 3. The 0-VHEAs have greater Young's modulus than the 0-NbHEAs, which may be affected by increasing the hardness and density values. In addition, the value of the Poisson ratio for 0-VHEA is the highest one. Young’s

Table 3 — The Youngs modulus values and Poisson ratios of the HEAs

HEAs	Poisson ratio (v)	E (GPa)
0-VHEA	0.238	145.2
0-NbHEA	0.164	133.7

modulus is between the stainless steel and Ti alloys and the Poisson ratio less than 0.3 in the two cases.

Materials with Poisson's ratios less than 0.3 are often considered to be "auxetic" materials. Auxetic materials exhibit unusual mechanical behavior where they expand laterally when stretched, contrary to the behavior of conventional materials that contract laterally when stretched. It's important to note that while auxetic materials with Poisson's ratios less than 0.3 have unique mechanical properties, their suitability for specific biomedical applications depends on a range of factors, including biocompatibility, durability, and other mechanical properties such as tensile strength and fatigue resistance. Therefore, the choice of materials for biomedical applications should be based on a comprehensive evaluation of all relevant factors[62,63].

3.4. Corrosion characteristics

3.4.1 WL Measurement

Figures 10-12 show the WL of the sintered VHEAs and NbHEAs in physiological media like AS, SBF, and HA, which are suitable for biomedical applications. The figures show that the corrosion rate (CR) for both NbHEAs and VHEAs increases in the three corrosive media by increasing the space holder ratio. This is because the porosity, either closed, open, or connected, increases by increasing the space holder percentage. This gives a greater chance for the corrosive agent to penetrate the surface of the samples, causing more chemical contact, and then the CR increases. Also, by increasing the immersion time, the CR increases due to increasing the time of corrosive medium diffusion inside the sample, leading to more chemical reactions. Another phenomenon

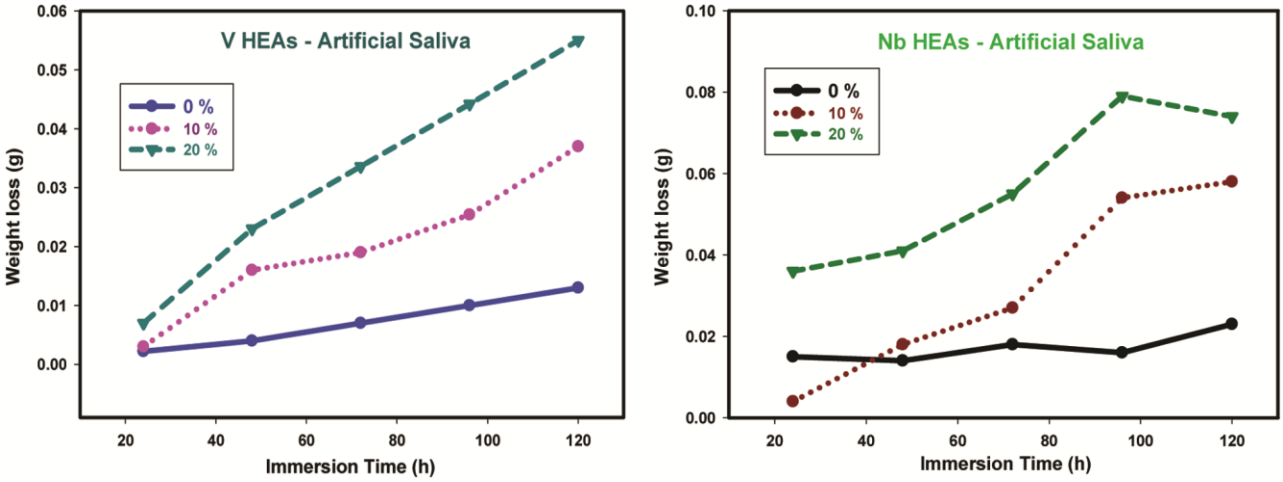

Fig. 10 — WL measurements vs. immersion times for porous VHEAs and NbHEAs in AS.

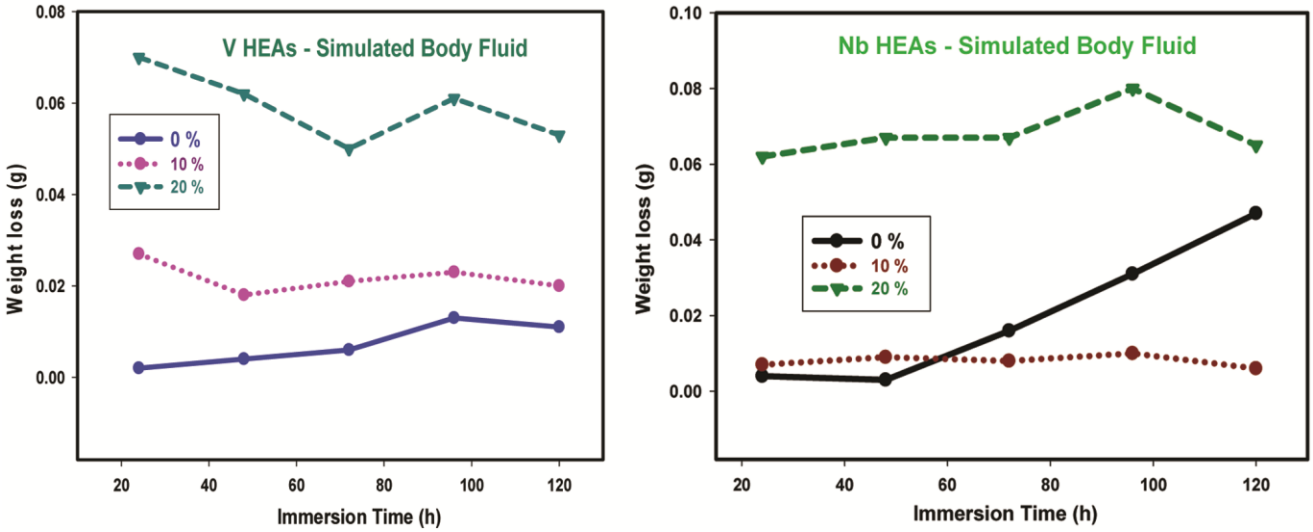

Fig. 11 — WL measurements vs. immersion times for porous VHEAs and NbHEAs in SBF.

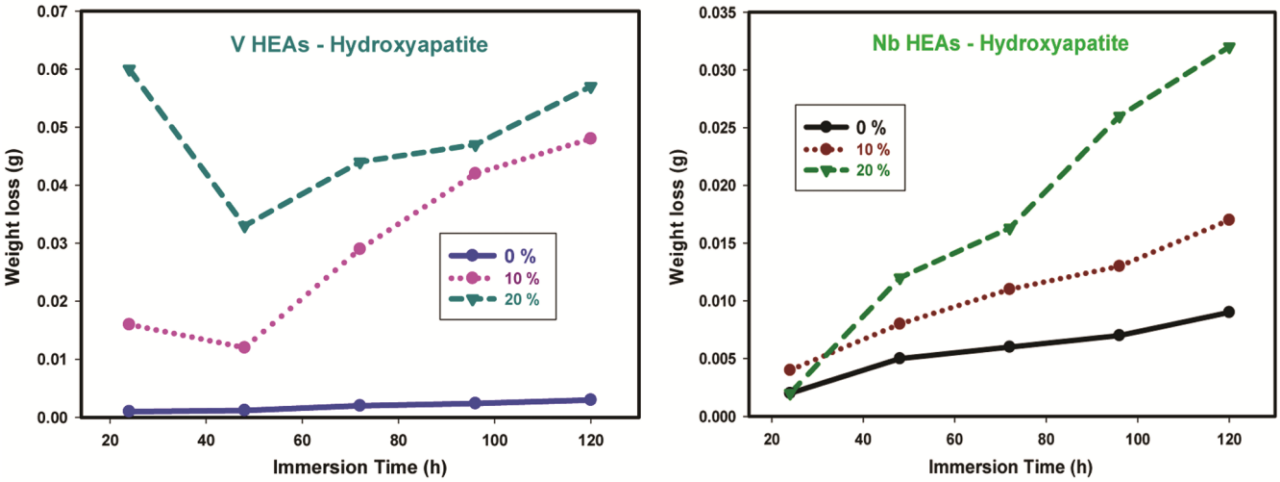

Fig. 12 — WL measurements vs. immersion times for porous VHEAs and NbHEAs in HA.

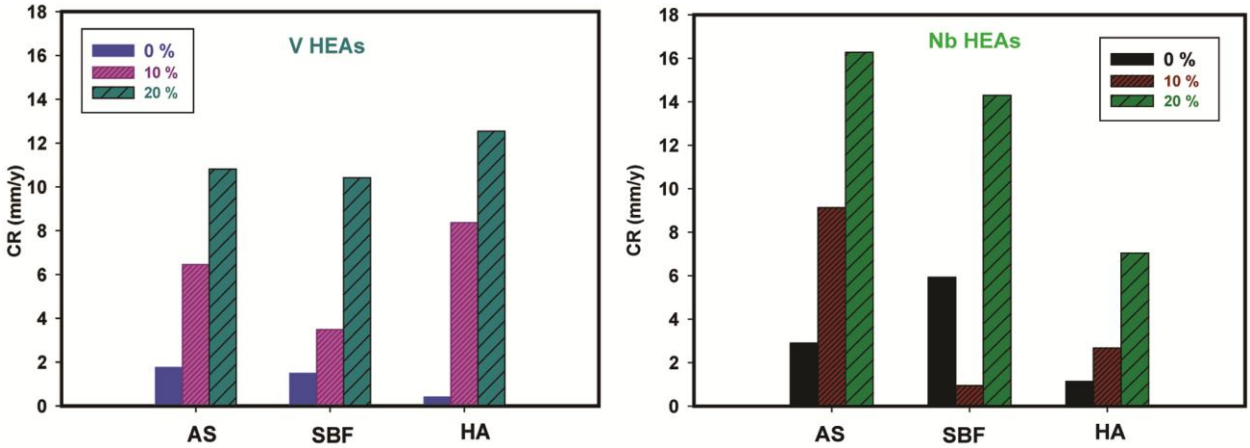

Fig. 13 — CR values for porous VHEAs and NbHEAs in physiological media.

observed from the figures is the increase in the CR values of NbHEAs compared to VHEAs. The WL values for 20-NbHEAs were larger because they exhibited less density than that of 20-VHEAs, as shown in Fig. 2. This may be attributed to the larger number of pores for NbHEAs, which is evident from the microstructure in Fig. 8. This gave the chance for a more significant amount of the corrosive medium to go into the sample, causing more WL values. Moreover, this can also be explained by the high electrochemical activity of V metal, which is higher than that of Nb metal. The electrochemical standard potential for vanadium is -1.17 V, which is less than -1.099 V for Nb, facilitating the formation of an oxide film of V_2O_3 on the pore surface and the sample surface. This acts as a protective layer for the VHEA from further corrosion. Moreover, the highest WL values were recorded for VHEA in the AS, followed by SBF, and the lowest values were recorded for (HA). However, for NbHEAs samples, the highest WL values were recorded for SBF, then (AS), and the lowest was for (HA).

Figure 13 provides the CR of the sintered VHEAs and NbHEAs in different physiological media like AS, SBF, and HA media for 120 h. A sharp rise in WL accompanied the increase of AHCs from 0% to 20 %, and the CR values reached their maximum (16.272 mm/y) for the 20-NbHEA specimen tested in AS. The reaction of Ti with the HA led to the synthesis of TiO_2, $CaTiO_3$, and TiP, which considerably enhanced the compactness of the coating[64]. The HA coating caused the CR to improve to 1.134 mm/y for 0-NbHEAs. In addition, after 5 days of immersing in the physiological media, the WL on the surface of the HEA composed of Ti and V/Nb percentages increased over time. The apatite's growth

on the coatings' surface improved by forming the Ti compounds due to the existence of HA. This was due to the formation of TiO_2, $CaTiO_3$, and TiP[64].

The irregularity of TiO_2 layers is caused by insufficient anodization time. The initial growth rate of this layer is much greater than the dissolution rate because the activity of titanium to create oxides in the electrolyte is still greater than that of those oxides to dissolve in the electrolyte. Therefore, the surface is locally stimulated, and random holes develop[65]. In the NbHEAs, better protection was developed on 0-NbHEAs in AS, 0-NbHEAs in HA, and 10-NbHEAs in SBF where CR values were 2.8, 1.13, and 0.94 mm/y, respectively. However, in the VHEAs, better protection was developed on 0-VHEAs in all media AS, HA, and SBF where CR values were 1.753, 0.4045, and 1.483 mm/y, respectively.

After only 2 days of immersion, the HA and AS formed a protective film in 0-NbHEAs. This conclusion may be attributed to the high passivation rate of the elements Ti, Ca, and P. As demonstrated in Figs. 10 and 12, steady curves were observed for all examined systems, indicating that the passivating coating generated at the metal-electrolyte interface was uniform and protective. For VHEAs, better protection exists at 20-VHEA in HA as shown in Fig. 13.

The HEA exhibited fluctuating values when submerged in the SBF medium. This may occur due to a certain degree of porosity, and the corrosion process of HA coatings can be altered correspondingly. In the case of HA, the type of substrate may also be associated with the sequential rise levels. When it comes to compositionally complex alloys, however, it is difficult to analyze the influence of each component element on corrosion performance in a particular environment[66]. As shown in Fig. 13, the CR reveals the degree of material degradation in a specific medium. The SBF had a negative effect on the proportion of AHCs, which increased CR values of HEA. Due to these factors, Ti implants are often covered with hydroxyapatite ($Ca_5(PO_4)_3(OH)$, HA), a bioceramic that matches the mineral components of human bones and teeth. HA would decrease the release of metallic ions by serving as a barrier and boosting the bioactivity of its chemical constituents[67]. The HA coating can only be a semi-insulating barrier to avoid solution-substrate contact. Corrosion is caused by the entry of chloride ions and water into the specimen, the transport of ions across the surface, and the ensuing electrochemical processes at HA contact. Zhang et al. discovered two phases in the corrosion process of HA with pores[68]. Firstly, hydrogen ions (H^+) are produced at the interface area where corrosion occurs:

$$Ti + 2H_2O \rightarrow TiO_2 + 4H^+ + 4e^- \quad \text{... (3)}$$

The dissolution of HA in the high H^+ concentration area is the next step:

$$Ca_{10}(PO_4)_6(OH)_2 + 2\,H^+ \rightarrow 10Ca^{2+} + 6PO_4^{3-} + H_2O \quad \text{... (4)}$$

The local pH of the contact is very low because H^+ cannot be effectively removed from the interface, accelerating HA's catalytic dissolution. Once corrosion has begun, it cannot be stopped until the whole interfacial HA has been dissolved. The coating then fails at the interface between the coating and substrate[68]. This corrosion process is consistent with the disparity in corrosion resistance between distinct HA coatings with differing degrees of porosity.

3.4.2 Surface Morphology

Figures 14-16 show the SEM images of the different sintered HEAs after immersion in AS, SBF, and HA media, respectively. As the AHCs increased, the CR of the VHEAs and NbHEAs increased in all conditions except the 10-NbHEAs. in Fig. 15. This is because of increasing pores, which facilitates corrosion attacks. The density of 0-VHEAs and 10-VHEAs is lower than 0-NbHEAs and 10-NbHEAs, respectively, but the WL and CR values are higher in the case of NbHEAs than in VHEAs, as shown in Fig. 14. Also, the density of 20-VHEAs is higher than 20-NbHEAs in line with WL and CR values. The NbHEAs have more localized corrosion than VHEAs, as indicated in Fig. 14, which was explained in the previous sections. The microstructure shows a smoother surface for VHEAs than that of NbHEAs. At 10-NbHEAs, the surface contains a protective layer on the pore surface contacting the SBF medium, as shown in Fig. 15(d), which decreases the CR value. At 20-NbHEAs, increasing AHCs led to cracks in the protective layer, as shown in Fig. 15(f), which has the lowest pitting and localized corrosion. The density value of 0-VHEAs is lower than 0-NbHEAs, respectively, but the WL and CR values are higher in the case of NbHEAs than in VHEAs, as shown in Fig. 16. The density value of 10-VHEAs is lower than 10-NbHEAs in line with WL and CR values and SM in Fig 16. The density value of 20-VHEAs is higher than 20-NbHEAs, which is reversed with higher WL

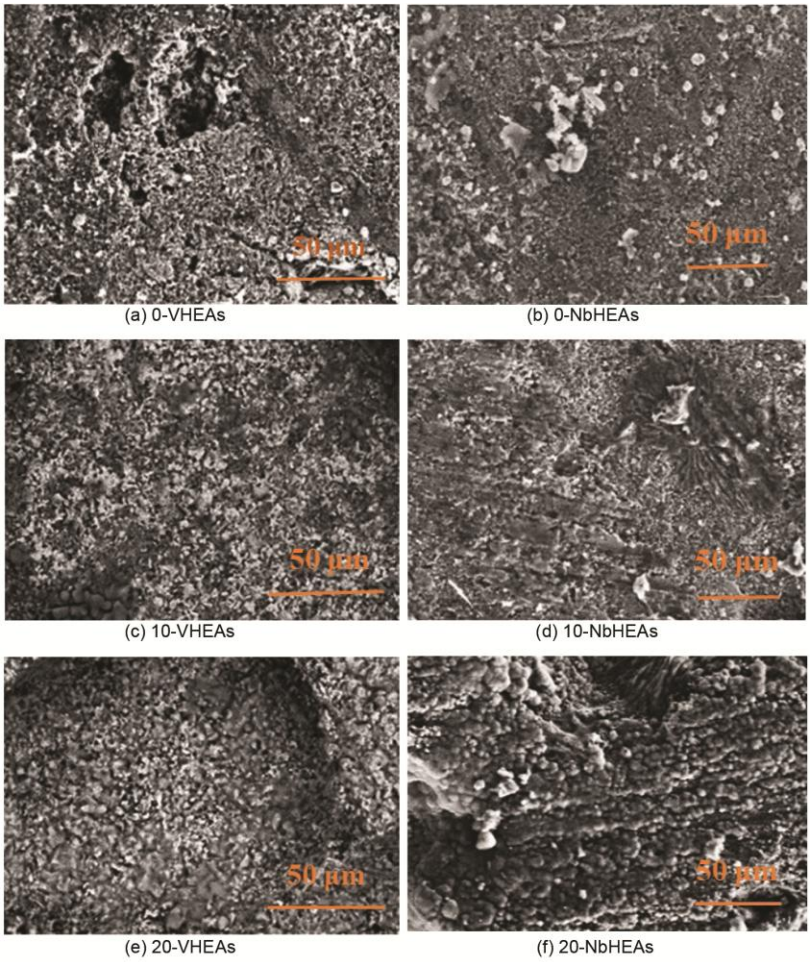

Fig. 14 — SEM micrographs of different sintered HEAs in AS.

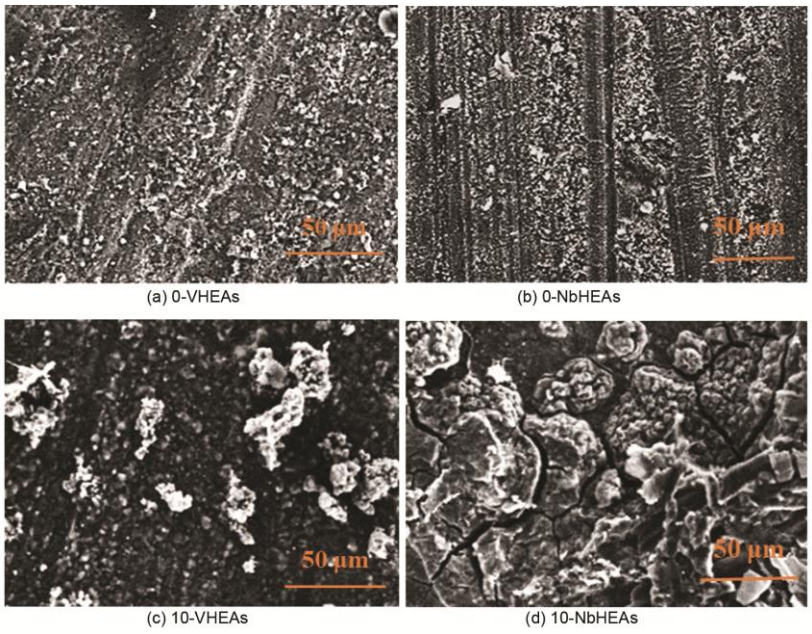

(*Contd*.)

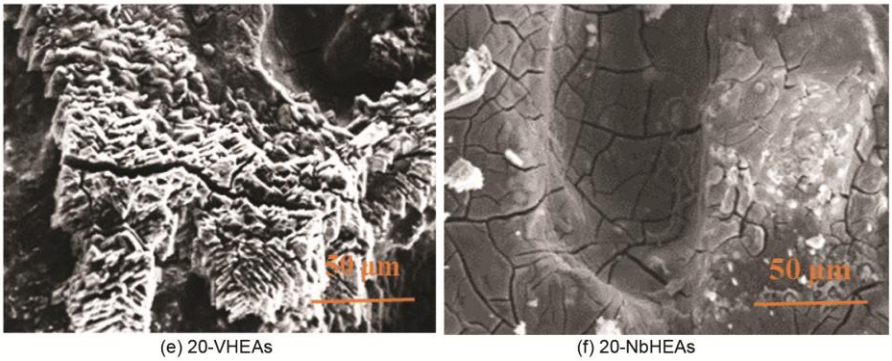

Fig. 15 — SEM micrographs of different sintered HEAs in SBF.

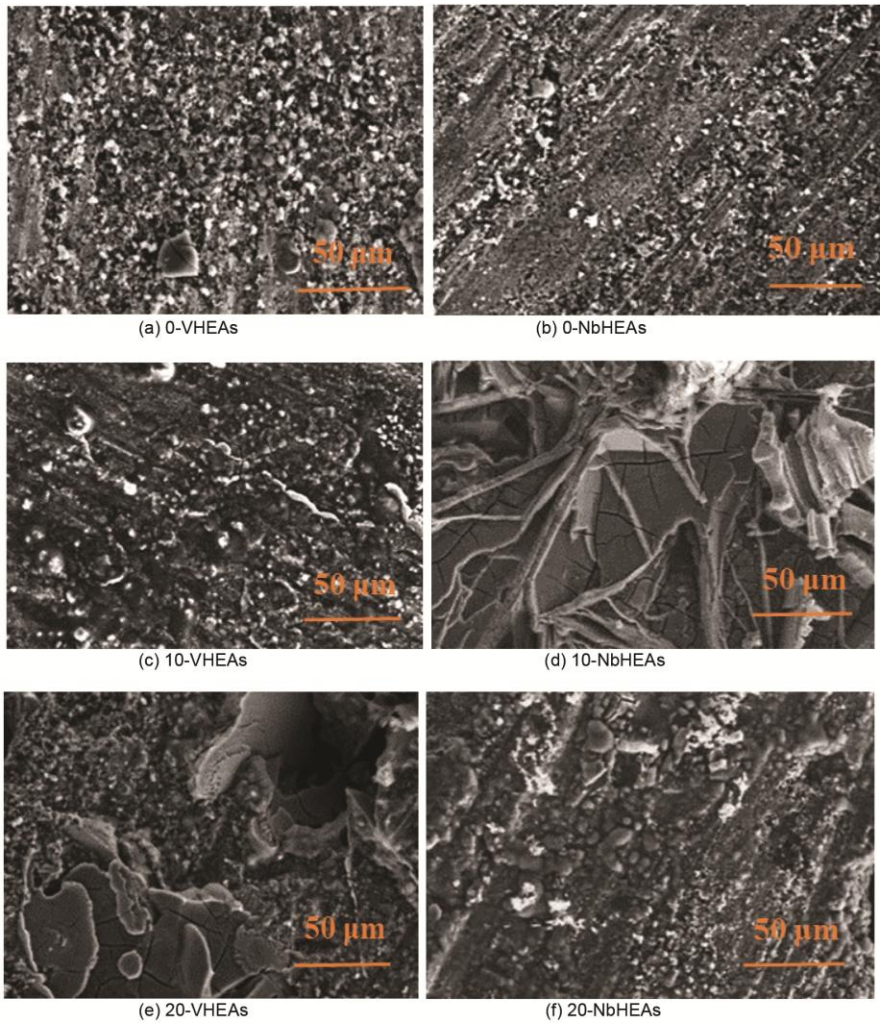

Fig. 16 — SEM micrographs of different sintered HEAs in HA.

and CR values. This might be due to the precipitation of protective corrosion products on 20-NbHEAs as for 10-NbHEAs, as clear from Figs 16 (d & f). The 10-NbHEAs and 20-VHEAs have lower pitting and localized corrosion than 10-VHEAs and 20-NbHEAs, as given in Fig. 16.

4 Conclusion

Porous TiMoCuAgV (VHEAs) and TiMoCuAgNb (NbHEAs) have been prepared via mechanical milling and PM technique using ammonium hydrogen carbonate (AHCs) as space holder material. The main characteristic is as follows:

1 Relative density is higher in the case of 0-NbHEAs and 10-NbHEAs compared to 0-VHEAs and 10-VHEAs. However, 20-VHEAs have a higher density than 20-NbHEAs. This is because of increasing the AHCs of the two- HEAs.
2 The SEM micrographs, EDX analysis, and mapping indicate a homogenous distribution for all the constituent phases in the two HEAs.
3 Uniform distribution for pores through the matrix of VHEAs compared to NbHEAs.
4 The hardness values are in line with the density values of the two HEAs. However, Young's modulus value of 0-VHEA is greater than that of 0-NbHEA.
5 The CR values increase as the HEAs are immersed in three physiological fluids for extended periods. When the AHCs percentage increased from 0% to 20%, there was a sharp increase in WL and CR. Generally, the VHEAs have better corrosion behavior than NbHEAs in all media. The CR values in AS media reached the highest at 20-NbHEAs, where they were 0.074 g and 16.272 mm/y, respectively.
6 The SM of VHEAs has lower pitting and localized corrosion than in the case of NbHEAs in all AHCs percentages in AS media. However, in SBF media, the 10-NbHEAs contain protective layers from the corrosion produced, giving lower pitting and localized corrosion compatible with WL and CR values. Also, in HA media, the 10-NbHEAs and 20-NbHEAs demonstrate a protective layer from the corrosion products, which aligns with the WL and CR values with lower pitting and localized corrosion.

Conflicts of interest

The authors declare that they have no conflicts of interest.

Data Availability

The data that support the findings of this study are available upon reasonable request from the authors.

References

1 Yang W, Pang S, Liu Y, Wang Q, Liaw P K & Zhang T, *Intermetallics*, 141 (2022) 107421.
2 Mohamed L Z, Elsayed A H, Elkady O A & Abolkassem S A, *J Mater Res Technol*, 24 (2023) 9897.
3 S Guo & Liu C T, *Prog Nat Sci: Mater Int*, 21 (2011) 433.
4 Ye Y F, Wang Q, Lu J, Liu C T & Yang Y, *Mater Today*, 19 (2016) 349.
5 Miracle D B & Senkov O N, *Acta Mater*, 122 (2017) 448.
6 Tang Z, Yuan T, Tsai C-W, Yeh J-W, Lundin C D & Liaw P K, *Acta Mater*, 99 (2015) 247.
7 Bartmanski M, Zielinski A, Majkowska-Marzec B & Strugala G, *Ceram Int*, 44 (2018) 19236.
8 Rodrigues J F Q, Costa D, Contieri R J, Osório W R, & Bortolozo A D, *Mater Sci Eng A*, 744 (2019) 305.
9 Bachani S K, Wang C-J, Lou B-S, Chang L-C & Lee J-W, *Surf Coat Technol*, 403 (2020) 126351.
10 Hengel I A J van, Tierolf M W A M, Fratila-Apachitei L E, Apachitei I & Zadpoor A A, *Int J Mol Sci*, 22 (2021).
11 Soare V, Burada M, Constantin I, Mitrică D, Bădiliță V, Caragea A & Târcolea M, *Appl Surf Sci*, 358 (2015) 533.
12 Varalakshmi S, Kamaraj M & Murty B S, *Metall Mater Trans A*, 41 (2010) 2703.
13 Wang C, Ji W & Fu Z, *Adv Powder Technol*, 25 (2014) 1334.
14 Chen Y L, Hu Y H, Tsai C W, Chen S K & Chang S Y, *Mater Chem Phys*, 118 (2009) 354.
15 Alaneme K K, Bodunrin M O & Oke S R, *J Mater Res Technol*, 5 (2016) 384.
16 Majumdar D D, Kumar V, Roychowdhury A, Mondal D P, Ghosh M & Nandi S K, *Materialia*, 9 (2020) 100623.
17 Gurel S, Yagci M B, Bal B & Canadinc D, *Mater Chem Phys*, 254 (2020) 123377.
18 Ramstedt M, Ekstrand-Hammarström B, Shchukarev A V, Bucht A, Österlund L, Welch M & Huck W T S, *Biomaterials*, 30 (2009) 1524.
19 Niinomi M, *Metall Mater Trans*, 33 (2002) 477.
20 Chen Q & Thouas G A, *Mater Sci Eng R Rep*, 87 (2015) 1.
21 Alamdari A A, Unal U & Motallebzadeh A, *Surf Interf*, (2021).
22 Kamachimudali U, Sridhar T M & Raj B, *Sadhana*, 28 (2003) 601.
23 Niinomi M, Nakai M & Hieda J, *Acta Biomater*, 8 (2012) 3888.
24 Popescu G, Ghiban B, Popescu C A, Rosu L, Trusca R, Carcea I, Soare V, Dumitrescu D, Constantin I, Olaru M T & Carlan B A, *IOP Conf Ser Mater Sci Eng*, 400 (2018).
25 Ghiban B, Popescu G, Lazar C, Rosu L, Constantin I, Olaru M & Carlan B, *IOP Conf Ser Mater Sci Eng*, 374 (2018).
26 Li J, Yang X, Zhu R & Zhang Y, *Metals*, 4 (2014) 597.
27 Bartolomeu F, Costa M M, Gomes J R, Alves N, Abreu C S, Silva F S & Miranda G, *Tribol Int*, 129 (2019) 272.
28 Ozan S, Lin J, Li Y, Ipek R & Wen C, *Acta Biomater*, 20 (2015) 176.
29 Kwak T Y, Yang J Y, Heo Y B, Kim S J, Kwon S Y, Kim W J & Lim D H, *J Mater Res Technol*, 10 (2021) 250.
30 Hua N, Wang W, Wang Q, Ye Y, Lin S, Zhang L, Guo Q, Brechtl J & Liaw P K, *J Alloys Compd*, 861 (2021) 157997.
31 Mutlu I & Oktay E, *Mater Sci Eng C*, 33 (2013) 1125.
32 Dimic I D, Cvijovic-Alagic I L, Kostic I T, Peric-Grujic A A, Rakin M P, Putic S S & Bugarski B M, *Chem Ind Chem Eng Q*, 20 (2014) 571.
33 Gunathilake T M S U, Ching Y C, Ching K Y, Chuah C H & Abdullah L C, *Polymers*, 9 (2017) 160.
34 Liang J, Li B & Wu L, *Soft Matter*, (2020).
35 Maksoud F J, Paz M F Vela´zquez de la, Hann A J, Thanarak J, Reilly G C, Claeyssens F, Green N H & Zhang Y S, *J Mater Chem B*, 10 (2022) 8111.
36 Domínguez-Trujillo C, Beltrán A M, Garvi M D, Salazar-Moya A, Lebrato J, Hickey D J, Rodríguez-Ortiz J A, Kamm P H, Lebrato C, García-Moreno F, Webster T J & Torres Y, *Surf Coat Technol*, 357 (2019), 896.

37 Hori T, Nagase T, Todai M, Matsugaki A & Nakano T, *Scripta Materialia*, 172 (2019) 83.
38 Ferrandini P L, Cardoso F F, Souza S A, Afonso C R, & Caram R, *J Alloys Compd*, 433 (2007) 207.
39 Zhou Y-L, Niinomi M & Akahori T, *Mater Sci Eng*, 483–484 (2008) 153.
40 Shi Y Z, Yang B & Liaw P K, *Metals*, 7 (2017) 43.
41 Zhou Q, Sheikh S, Ou P, Chen D, Hu Q & Guo S, *Electrochem Commun*, 98 (2019) 63.
42 Wang Q, Han C, Choma T, Wei Q, Yan C, Song B & Shi Y, *Mater Des*, 126 (2017) 268.
43 Hempel F, Finke B, Zietz C, Bader R, Weltmann K D & Polak M, *Surf Coat Technol*, 256 (2014) 52.
44 Cai D, Zhao X, Yang L, Wang R, Qin G, Chen D & Zhang E, *J Mater Sci Technol*, 81 (2021) 13.
45 Ewald A, Glückermann S K, Thull R & Gbureck U, *Biomed Eng Online*, 5 (2006) 1.
46 Gurappa I, Mater Char, 49 (2002) 73.
47 Vidal C V & Mu~Noz A I, *Electrochim Acta*, 56 (2011) 8239.
48 Rincic N, Baucic I, Miko S, Papic M & Prohic E, *Coll Antropol*, 27 (2003) 99.
49 Hurlbutt M, Novy B & Young D, *J Calif Dent Hyg Assoc*, 25 (2010) 9.
50 Motallebzadeh A, Peighambardoust N S, Sheikh S, Murakami H, Guo S & Canadinc D, *Intermetallics*, 113 (2019) 106572.
51 Taha R H, Gaber G A, Mohamed L Z & Ghanem W A, *Egypt J Chem*, 62 (2019) 367.
52 Abolkassem S A, Mohamed L Z, Gaber G A & Elkady O A, *J Mater Res Technol*, 10 (2021) 1122.
53 Disegi J A, Kenned R L & Pilliar R, *Danvers A*, (1999).
54 Chen Y, Liu W, Wang H, Xie J, Zhang T, Yin L & Huang Y, *Entropy*, 24 (2022) 241.
55 Hassan M A, Ghayad I M, Mohamed A S A, El-Nikhaily A E & Elkady O A, *J Mater Res Technol*, 13 (2021) 463.
56 Guo S, Ng C, Lu J & Liu C, *J Appl Phys*, 109 (2011) 103505.
57 Rodrigues J F Q, Costa D, Contieria R J, Osório W R & Bortolozo A D, *Mater Sci Eng A*, 744 (2019) 305.
58 Majumdar D D, Kumar V, Roychowdhury A, Mondal D P, Ghosh M & Nandi S K, *Materialia*, 9 (2020) 100623.
59 Hua N, Wang W, Wang Q, Ye Y, Lin S, Zhang L, Guo Q, Brechtl J & Liaw P K, *J Alloys Compd*, 861 (2021) 157997.
60 Li Y, Yang C, Zhao H, Qu S, Li X & Li Y, *Materials*, 7 (2014) 1709.
61 Kovacik J, *J Mater Sci*, 41 (2006) 1247.
62 Elipe J C A & Lantada A D, *Smart Mater Struct*, 21 (2012).
63 Momoh E O, Jayasinghe A, Hajsadeghi M, Vinai R, Evans K E, Kripakaran P & Orr J, *Thin-Walled Struct*, 196 (2024) 111447.
64 Maleki-Ghaleh H & Khalil-Allafi J, *Surf Coat Technol*, 363 (2019) 179.
65 Parcharoen Y, Kajitvichyanukul P, Sirivisoot S & Termsuksawad P, *Appl Surf Sci*, 311 (2014) 54.
66 Codescu M M, Vladescu A, Geanta V, Voiculescu I, Pana I, Dinu M, Kiss A E, Braic V, Patroi D, Marinescu V E & Iordoc M, *Surf Interf*, 28 (2022) 101591.
67 Kwok C T, Wong P K, Cheng F T & Man H C, *Appl Surf Sci*, 255 (2009) 6736.
68 Zhang Z, Dunn M F, Xiao T D, Tomsia A P & Saiz E, Nanotech Biotech Convergence – 2002 Stamford, CT, (2002) 291.